

Effective spin-1 breathing kagome Hamiltonian induced by the exchange hierarchy in the maple leaf mineral bluebellite


Pratay Ghosh ^{1,2}, Tobias Müller ¹, Yasir Iqbal ³, Ronny Thomale ^{1,3} and Harald O. Jeschke ^{3,4}

¹*Institut für Theoretische Physik und Astrophysik and Würzburg-Dresden Cluster of Excellence ct.qmat, Julius-Maximilians-Universität Würzburg, Am Hubland Campus Süd, Würzburg 97074, Germany*

²*Institute of Physics, Ecole Polytechnique Fédérale de Lausanne (EPFL), CH-1015 Lausanne, Switzerland*

³*Department of Physics and Quantum Centre of Excellence for Diamond and Emergent Materials (QuCenDiEM), Indian Institute of Technology Madras, Chennai 600036, India*

⁴*Research Institute for Interdisciplinary Science, Okayama University, Okayama 700-8530, Japan*

 (Received 18 January 2023; revised 14 March 2023; accepted 14 August 2024; published 3 September 2024)

The Heisenberg quantum antiferromagnet on the maple leaf lattice has been shown to feature highly exotic phases, and therefore material realizations are intensely sought after. We determine the magnetic Hamiltonian of the copper mineral bluebellite using density-functional theory based energy mapping. Due to significant distortion of the spin-1/2 maple leaf lattice, we find two of the five distinct nearest-neighbor couplings to be ferromagnetic. The solution of this Hamiltonian with density matrix renormalization group calculations points us to the surprising insight that this particular imperfect maple leaf lattice, due to the strongly ferromagnetic Cu^{2+} dimer, realizes an effective $S = 1$ breathing kagome Hamiltonian. In fact, this is another highly interesting Hamiltonian that has rarely been realized in materials. Analysis of the effective model within a bond-operator formalism then allows us to identify a valence bond solid ground state and extract thermodynamic quantities using a low-energy bosonic mean-field theory. We resolve the puzzle of the apparent one-dimensional character of bluebellite as our calculated specific heat has a Bonner-Fisher-like shape, in good agreement with the experiment.

DOI: [10.1103/PhysRevB.110.094406](https://doi.org/10.1103/PhysRevB.110.094406)

I. INTRODUCTION

Triangular motifs in quantum antiferromagnets are a source of geometric frustration that lead to highly nontrivial emergent phenomena like residual entropy, algebraic or dipolar correlations, spin liquids, spin nematics, etc. [1–4]. Starting from the triangular lattice (highest packing density in two dimensions), site depletion creates new lattices with potentially more frustration [5,6]. For example, the kagome lattice is obtained by a 1/4 site depletion of the triangular lattice; it also hosts some of the most intensively studied spin liquid candidates [7]. Similarly, the maple leaf lattice is a one-seventh site-depleted (one-sixth bond depleted) triangular lattice and has a coordination number of five [8]. The uniform nearest-neighbor Heisenberg antiferromagnetic model on this lattice was addressed numerically [9–14], and presumably, it has a magnetically ordered ground state. In their analytical work on a related model, Ghosh *et al.* established an exact dimer ground state [15], making it the only other two-dimensional lattice with uniform tiling that can host an exact dimer ground state, besides the celebrated Shastry-Sutherland model [16–20]. While $\text{SrCu}_2(\text{BO}_3)_2$ exemplifies the Shastry-Sutherland Hamiltonian [21], a realization of the maple leaf model proposed in Ref. [15] is yet to be identified. Candidates involving quantum spins are the copper minerals [22,23] spangolite $\text{Cu}_6\text{Al}(\text{SO}_4)(\text{OH})_{12}\text{Cl} \cdot 3\text{H}_2\text{O}$ [24], sabelite $\text{Cu}_2\text{ZnAsO}_4(\text{OH})_3$ [25], mojaveite $\text{Cu}_6\text{TeO}_4(\text{OH})_9\text{Cl}$ [26], fuettererite $\text{Pb}_3\text{Cu}_6\text{TeO}_6(\text{OH})_7\text{Cl}_5$ [27], and finally

bluebellite $\text{Cu}_6\text{IO}_3(\text{OH})_{10}\text{Cl}$ [26]. Magnetic properties have been characterized experimentally for spangolite [28] and bluebellite [29], but their magnetic Hamiltonians remain to be established.

Here, we focus on bluebellite and attempt to resolve some of the pressing issues for this layered maple leaf antiferromagnet: first, we determine all relevant exchange interactions of the system. The resulting Hamiltonian is dominated by the intralayer couplings. We then focus on the Hamiltonian corresponding to a single layer and employ numerical and semianalytical techniques. We also address the question raised by the experiment: why does bluebellite appear to have a Bonner-Fisher type behavior, suggestive of one-dimensional systems? An answer based on order-by-disorder was attempted without a knowledge of the Hamiltonian [30]. Methodologically, we apply the energy mapping technique which has proved valuable in extracting the Hamiltonian for many quantum spin systems [31–34]. By virtue of a statistical approach and by extracting more than the seemingly important exchange interactions, this method has led to valuable insights for many materials [35–41]. Using density matrix renormalization group (DMRG) calculations [42], we find that the resulting maple leaf Hamiltonian for bluebellite (in the absence of inter-layer couplings) results in a gapped valence bond solid (VBS) ground state. Furthermore, we develop an effective low-energy bosonic theory via bond operator formalism [43], obtain static and dynamical spin structure factors, and assess thermodynamic properties. We find that

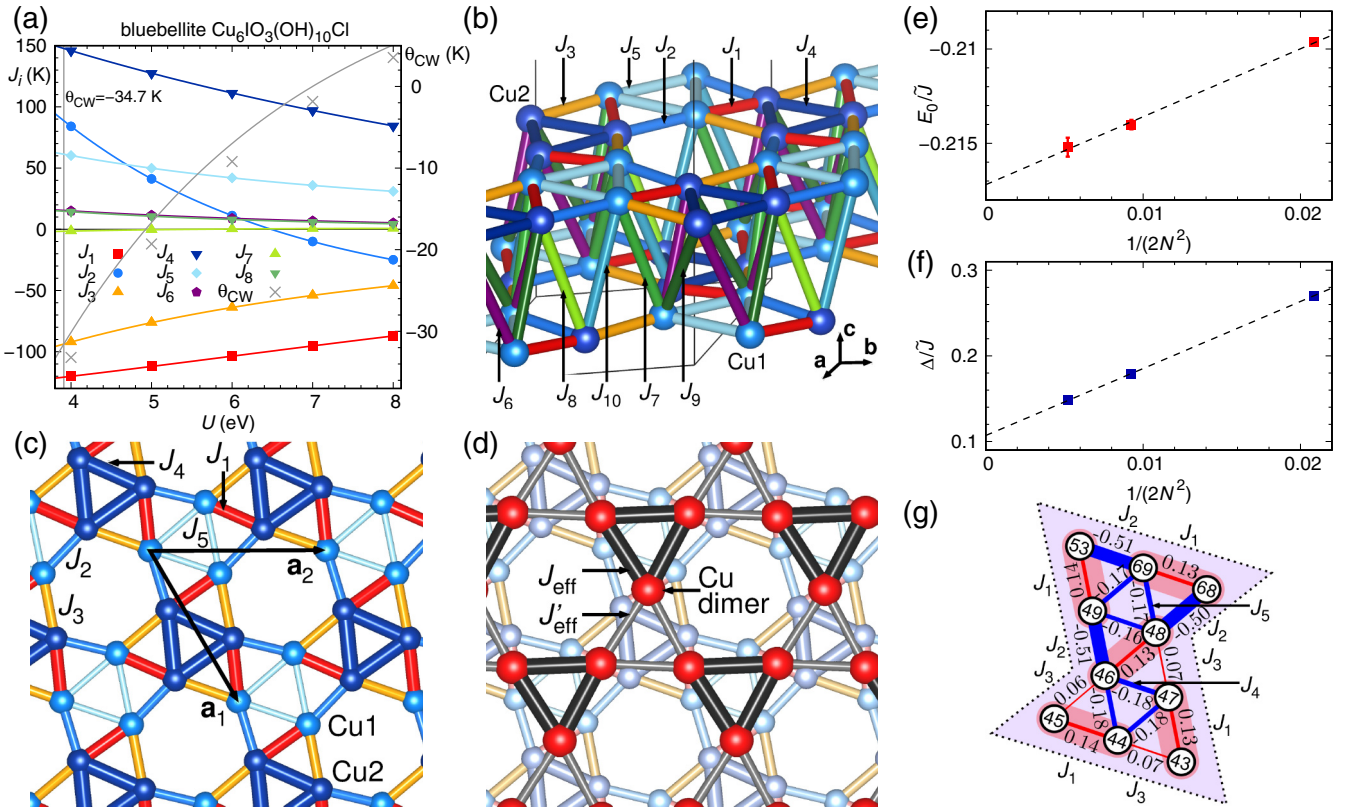


FIG. 1. (a) First eight exchange interactions of bluebellite as a function of on-site interaction strength U , at fixed Hund's rule coupling $J_H = 1$ eV. The vertical line indicates the U value at which the Heisenberg Hamiltonian parameters yield the experimentally observed Curie-Weiss temperature [29]. (b) Illustration of the first ten exchange paths, including the interlayer paths J_6 to J_{10} . (c) Bluebellite structure with the five “nearest-neighbor” exchange paths defining the maple leaf lattice. The lattice vectors are given by \mathbf{a}_1 and \mathbf{a}_2 . (d) Effective $S = 1$ breathing kagome model with renormalized interactions. (e) Ground state energy per site found in DMRG for system sizes $N = 48, 108, 192$. The ground state energy in the thermodynamic limit is estimated (via finite size scaling) to be $E_0/\tilde{J} \approx -0.217(1)$ per site using the energy scale of $\tilde{J} = \sqrt{J_1^2 + J_2^2 + J_3^2 + J_4^2 + J_5^2} = 238$ K. (f) Scaling of the spin-gap Δ in units of \tilde{J} . (g) Spin-spin correlations on a ten site cluster in the bulk obtained from DMRG on a 108 site maple leaf system. The thickness of the bonds indicates the strength of the correlation and the color red (blue) indicates positive (negative) correlation. Note the clear dimerization in the ground state.

the bluebellite intralayer magnetic interactions emulate an effective $S = 1$ kagome Hamiltonian with a strong breathing anisotropy, which is known to have a magnetically disordered ground state [44]. Bluebellite, however, shows a magnetic ordering at low temperatures [29]. This magnetic order, can, in principle, be linked to the weak intra- and interlayer couplings. Nonetheless, our interest here is the highly frustrated in-layer physics of bluebellite, the ground state of which relates to the strongly fluctuating state above the ordering temperature, and, possibly, to an effective spin-1 breathing kagome antiferromagnet. So far, the $S = 1$ kagome candidates, e.g., $\text{KV}_3\text{Ge}_2\text{O}_9$ [45], $\text{NaV}_6\text{O}_{11}$ [46], $m\text{-MPYNN} \cdot \text{BF}_4$ [47], all undergo lattice distortions at low temperatures. By establishing the connection between maple leaf and kagome, we pave the way to possible realizations and synthesis of new effective $S = 1$ kagome compounds emerging out of $S = 1/2$ maple leaf systems. As an experimental outlook, this enables the study of integer-spin kagome antiferromagnets, notably their magnetization plateaus, excitations, and topological properties.

II. MODEL HAMILTONIAN

To extract the parameters of the Heisenberg Hamiltonian $\hat{\mathcal{H}} = \sum_{i < j} J_{ij} \mathbf{S}_i \cdot \mathbf{S}_j$ for bluebellite, we relax the internal positions of H, O and Cl while keeping Cu and I positions and the lattice parameters fixed; this is necessary to sort out obvious distortions in the experimentally determined room temperature structure [29] (see Appendix A). Note that the maple leaf lattice structure in synthetic bluebellite is more regular compared to the structure of the mineral [26]. In the energy mapping technique, we make no assumptions about the important exchange paths. Rather, we determine 20 couplings up to Cu-Cu distances of 5.9 \AA (about twice the nearest-neighbor distance). In Fig. 1(a), we show how the first eight Heisenberg Hamiltonian parameters evolve with on-site Coulomb interaction U applied to the strongly correlated $\text{Cu}^{2+} 3d$ orbitals. The relevant U value is determined by calculating the Curie-Weiss temperature as $\theta_{\text{CW}} = -\frac{1}{3}S(S+1) \sum_i z_i J_i$ where z_i are the coordination numbers of J_i and demanding that it matches the experimentally observed value $\theta_{\text{CW}} = -34.7$ K [29].

The result for the five most dominant couplings in Fig. 1(a) is $J_1 = -120.8(1.3)$ K, $J_2 = 88.6(1.2)$ K, $J_3 = -93.7(1.0)$ K, $J_4 = 147.6(1.3)$ K, and $J_5 = 61.3(7)$ K constructing the maple leaf layers in Fig. 1(c). The rest of the couplings, both intra- and interlayer, e.g., $J_6 = 15.4$ K, $J_7 = -1.6$ K, $J_8 = 14.7$ K, $J_{18} = 14.6$ K, and $J_{20} = 12.6$ K are significantly weaker than the intra-layer couplings mentioned above (see Appendix A for more details), and are not included in our analyses. At first glance, it seems disappointing that the ferromagnetic interactions distance this two-dimensional (2D) Hamiltonian from the maple leaf model [15,48]. But, as we will reveal, these mixed ferro- and antiferromagnetic (FM and AFM) couplings engender enticing features. To begin with, the strongest AFM J_4 coupling would try to enforce a 120° order on the J_4 triangles, however, it might prove insufficient in establishing full magnetic order since the J_5 bonds, which form the other set of triangles, are the weakest. Furthermore, the second strongest AFM J_2 bonds and the FM J_3 bonds form hexagons, a structure of alternating interactions that is likely to promote dimerization. Finally, the strong FM J_1 bonds might try to project effective spin-1 onto them and reduce the quantum fluctuations. We now attempt to understand these intricacies that make the properties of bluebellite intriguing.

III. GROUND STATE

First, we study the ground state of the bluebellite Hamiltonian consisting of the intralayer magnetic interactions with DMRG using the iTENSOR library [49]. Based on finite-size-scaling of results from 48, 108, and 192 site clusters with 24 – 30 sweeps and a maximum bond dimension of 2048 [$U(1)$], we find a magnetically disordered ground state with an energy per site $E_0/\tilde{J} = -0.217(1)$, and a spin-gap of $\Delta/\tilde{J} = 0.107(1)$ with $\tilde{J} = \sqrt{J_1^2 + J_2^2 + J_3^2 + J_4^2 + J_5^2} = 238$ K [please refer to Figs. 1(e) and 1(f)]. The spin-spin correlations, $\langle \mathbf{S}_i \cdot \mathbf{S}_j \rangle$, for nearest-neighbor spin pairs \mathbf{S}_i and \mathbf{S}_j , show strong singlet formation on the AFM J_2 bonds [see Figs. 1(g) and 6 in Appendix B]. This propensity to form dimers on the J_2 bonds is indicative of a VBS ground state.

For a dimerized system, crucial insights can be obtained from the bond operator formalism [43], where one uses a dimer basis and writes the singlet and three triplets on a bond (here the J_2 bond) as bosons. We assume a singlet background (a product state of singlets on the J_2 bonds) as a mean field, and the triplon (dispersing triplet) excitations on the singlet are treated systematically while ignoring triplon-triplon interaction (details in Appendix C). This approach successfully describes several magnetic materials [50–54]. The results from this theory corroborate the DMRG calculations, it finds a stable VBS ground state with energy $E_0/\tilde{J} = -0.22494$ and a spin-gap $\Delta/\tilde{J} = 0.13474$ in the thermodynamic limit. The spin-spin correlations also agree with the DMRG results; the strongest, for example, is found to be -0.57570 on the J_2 bonds [compare with Fig. 1(g)].

Besides the strong singlets on the AFM J_2 bonds, the spins connected by FM J_1 interactions develop strong FM correlations. The total spin moment on the J_1 bonds is found to be ~ 1.8 in both methods, signaling the system's

tendency to form triplets on them and project onto an effective $S = 1$ (for full $S = 1$ projection, the total spin moment $S(S + 1) = 2$ on a bond). Thus, we discover that the bluebellite Hamiltonian mimics an effective $S = 1$ kagome system with breathing anisotropy (broken inversion symmetry) [55], with $J_{\text{eff}} \approx J_2 + J_5$ for smaller triangles, and $J'_{\text{eff}} \approx J_3 + J_4$ for larger triangles [see Fig. 1(d)]. We have evaluated the interactions in the effective $S = 1$ breathing kagome by repeating the energy mapping with $S = 1/2$ moments connected by J_1 bonds constrained to $S = 1$ (see Appendix A). We find AFM couplings $J_{\text{eff}} = 49(2)$ K and $J'_{\text{eff}} = 18(2)$ K, and the breathing anisotropy is $J_{\text{eff}}/J'_{\text{eff}} \approx 2.7$ [Fig. 1(d)].

Reference [44] furnishes an understanding of the ground state of the $S = 1$ breathing kagome AFM. For isolated J_{eff} triangles ($J'_{\text{eff}} \rightarrow 0$) the ground state is a product of singlets on each J_{eff} triangle. With $J'_{\text{eff}} \neq 0$, triplet fluctuations develop, which, for $J'_{\text{eff}} \leq J_{\text{eff}}$, remain insufficient to close the spin gap, and thus, a trimerized singlet ground state stabilizes [44,56,57]. In our case, a similar trimerized state is also realized, which materializes continuously from the dimerized state when $J_1 \rightarrow \infty$, i.e., the spin-1/2's across the J_1 bond get exactly projected to spin-1. The dimerized state here is akin to the VBS state (Haldane state [58]) for the AFM spin-1 chain due to Affleck, Kennedy, Lieb, and Tasaki [59]. In both cases, one sees the spin-1 as a combination of two spin-1/2, tries to satisfy the AFM interactions locally, and then projects a spin-1 out of two spin-1/2. Starting from the J_1 - J_2 only limit, the ground state of bluebellite can be interpreted as a product state of three spin Haldane states with J_2 coupling, which gets renormalized by other interactions. Such an effective spin-1 resulting out of a pair of spin-1/2 leading to a spin-gapped ground state was also seen in Ref. [53], where spin-1 kagome emerges out of a $S = 1/2$ honeycomb system.

IV. STATIC AND DYNAMICAL STRUCTURE FACTORS

We calculate the static structure factor,

$$S(\mathbf{q}) = \frac{1}{N} \sum_{ij} e^{i\mathbf{q} \cdot (\mathbf{r}_i - \mathbf{r}_j)} \langle \mathbf{S}_i \cdot \mathbf{S}_j \rangle, \quad (1)$$

using DMRG and bosonic theory. The DMRG result [Fig. 2(a)] shows diffused peaks at the M points of the fourth Brillouin zone (BZ). In contrast, the peaks from the bosonic theory [Fig. 2(b)] are shifted from the M points. To understand this, we exploit the relation between the kagome and the maple leaf lattice [see Fig. 2(c)], to transform the $S_{\mathbf{q}}$ of the kagome $\mathbf{q} = 0$ order state into the $S_{\mathbf{q}}$ for maple leaf via a basis expansion. The static structure factor for a non-Bravais system like kagome and maple leaf can be written as

$$S(\mathbf{q}) = \frac{1}{N} \sum_{ij} \sum_{kk'} e^{i\mathbf{q} \cdot [(\mathbf{R}_i - \mathbf{R}_j) + (\mathbf{v}_k - \mathbf{v}_{k'})]} \times \langle \mathbf{S}_{k'}(\mathbf{R}_j) \cdot \mathbf{S}_k(\mathbf{R}_i) \rangle, \quad (2)$$

where \mathbf{R}_i are the positions of the unit cells, and \mathbf{v}_k are the basis vectors. To transform the kagome unit cell into the maple leaf unit cell one needs to expand each basis site of kagome into two sites [see Fig. 2(c)]. For the k th basis site of kagome, this is achieved by creating two sites at $\mathbf{v}_k \pm \vec{\delta}_k$. The $\vec{\delta}_k$'s are given in Fig. 2(c). Thereafter, the static structure factor for the maple

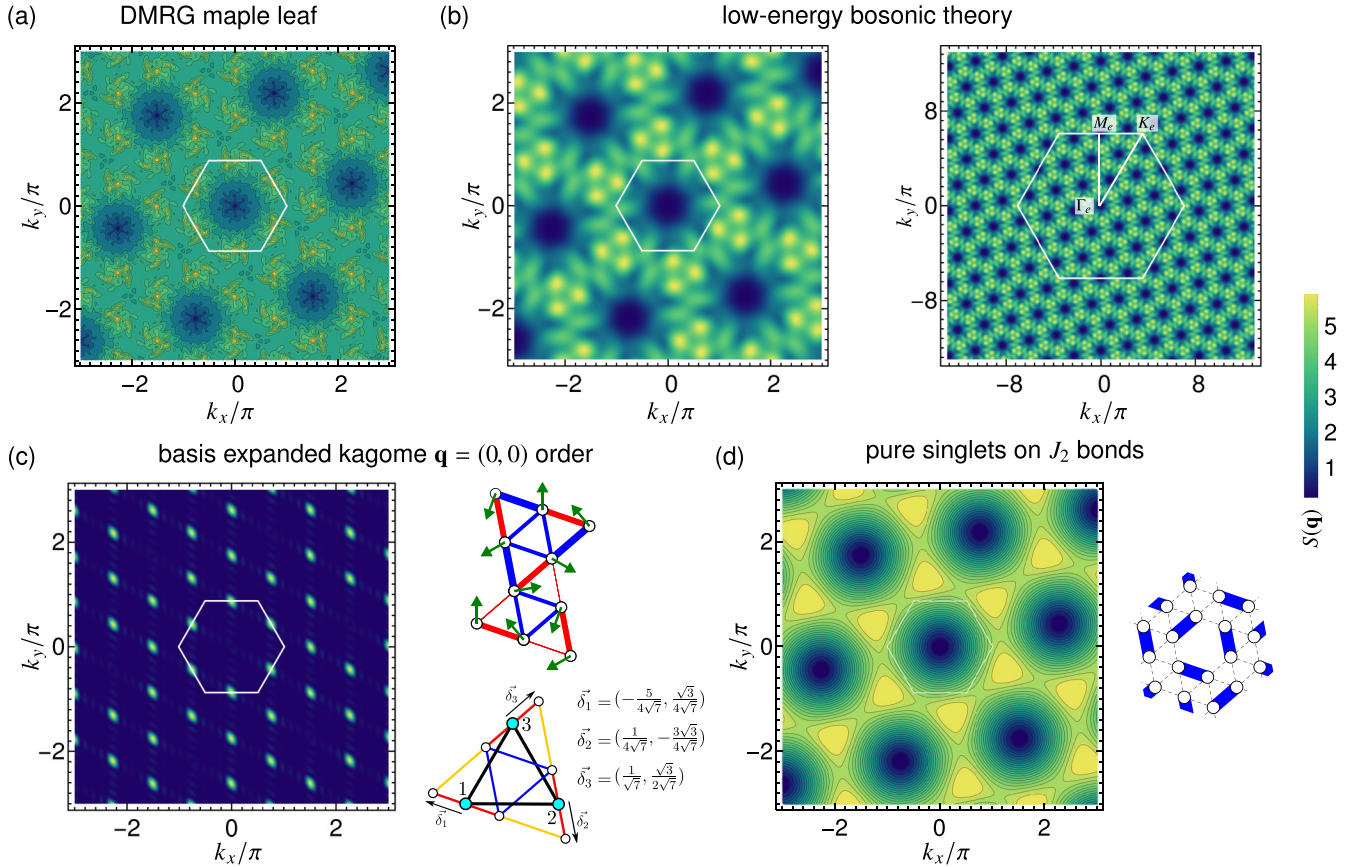


FIG. 2. Static spin structure factor, $S_{\mathbf{q}}$, obtained from (a) DMRG on a 192 site maple leaf cluster, (b) bond operator theory. (c) The $S_{\mathbf{q}}$ for the maple leaf lattice obtained via a basis expansion [see Eq. (2)] of the kagome $\mathbf{q} = 0$ order. We also introduce a relative canting between the spins across the FM J_1 bonds as shown in the spin configuration. The Bragg peaks at the M points of the fourth BZ remains unchanged by the relative canting. (d) The $S_{\mathbf{q}}$ for a product state of pure singlets on the J_2 bonds (see Fig. 8 in Appendix C). The soft maxima of $S_{\mathbf{q}}$ now appear shifted away from the M points.

leaf lattice is derived from the spin-spin correlations of the kagome system as

$$S(\mathbf{q}) = \frac{1}{N} \sum_{ij} \sum_{kk'} e^{i\mathbf{q} \cdot [(\mathbf{R}_i - \mathbf{R}_j) + (\mathbf{v}_k - \mathbf{v}_{k'}) + (\pm \vec{\delta}_k \mp \vec{\delta}_{k'})]} \times \langle \mathbf{S}_{k'}(\mathbf{R}_j) \cdot \mathbf{S}_k(\mathbf{R}_i) \rangle. \quad (3)$$

Figure 2(c) shows a result for classical spins for which the ground state is known to be degenerate with both $\mathbf{q} = 0$ and $\sqrt{3} \times \sqrt{3}$ coplanar orders. For a $\sqrt{3} \times \sqrt{3}$ order, the peaks occur at the K points, while for $\mathbf{q} = 0$ order, they occur at the M points of the extended BZ of the kagome lattice. Here the maple leaf spins that are across the FM J_1 bonds, i.e., the ones that emerged from the same kagome spin in the basis transformation, are assumed parallel to each other, however, even with a relative canting, the Bragg peaks remain at the M points [see Fig. 2(c)]. As the shifted peaks in Fig. 2(b) cannot be explained classically, they must have a quantum mechanical origin. We see that a product state of singlets on the J_2 bonds (the bare mean-field wave function for our bosonic theory) reproduces the shift in question [Fig. 2(d)] signaling the relevance of the stabilization of singlets on the J_2 bonds. The other modifications seen in Fig. 2(b) are ascribed to triplet fluctuations.

The shift in the peaks results in an enlargement of the BZ of the $S_{\mathbf{q}}$ [Figs. 2(b) and 3(b)]. The form factor, $f_{\mathbf{G}}$, for a maple leaf system is given by $f_{\mathbf{G}} \propto \sum_j \exp(i\mathbf{G} \cdot \mathbf{v}_j)$ where \mathbf{v}_j are the six basis vectors of the lattice, $\mathbf{G} = \nu_1 \mathbf{b}_1 + \nu_2 \mathbf{b}_2$ with reciprocal vectors \mathbf{b}_1 and \mathbf{b}_2 (ν_1 and ν_2 are integers). The maxima of $|f_{\mathbf{G}}|^2$ occur for $\text{mod}(\nu_1 + 2\nu_2, 7) = 0$, i.e., by traversing along \mathbf{b}_1 or \mathbf{b}_2 , the structure factor is only periodic in seven reciprocal lattice spacings. Therefore, the extended BZ of the structure factor is seven times larger than the actual BZ of the lattice [see Fig. 2(b)]. This significantly enlarged extended BZ is the reason behind the disagreement between the $S(\mathbf{q})$ from finite-size DMRG and the one from bond-operator mean-field theory in the thermodynamic limit.

We further calculate the powder averaged static spin structure factor, $S(Q) = \frac{1}{4\pi} \int d\Omega_{\mathbf{q}} S(\mathbf{q})$, with $Q = |\mathbf{q}|$, from both DMRG and bond operator mean-field theory. We show the magnetic form factor, $F(Q)$, modulated $S(Q)$ in Fig. 3(a). Here,

$$F(Q) = 0.0232e^{-34.969(\frac{Q}{4\pi})^2} + 0.4023e^{-11.564(\frac{Q}{4\pi})^2} + 0.5882e^{-3.843(\frac{Q}{4\pi})^2} - 0.0137 \quad (4)$$

for Cu^{2+} ions [60]. Apart from the static spin structure factor, we also compute the dynamical spin structure factor,

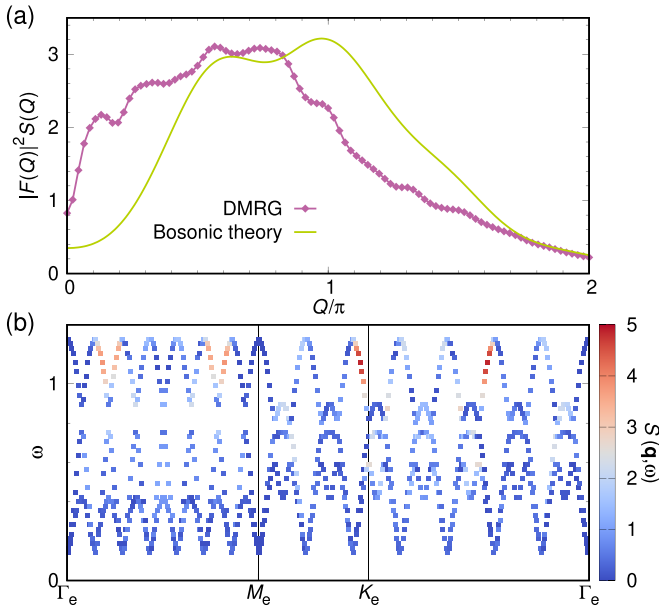


FIG. 3. (a) Form factor modulated powder averaged static structure factor obtained from DMRG and bond-operator mean-field theory. (b) Dynamical spin structure factor from bond-operator mean-field theory. $S(\mathbf{q}, \omega)$ shows the typical behavior of a magnetically disorder system with gapped and dispersive triplet excitation.

$S(\mathbf{q}, \omega) = \frac{1}{N} \sum_{ij} e^{i\mathbf{q} \cdot (\mathbf{r}_i - \mathbf{r}_j)} \int_{-\infty}^{\infty} dt e^{i\omega t} \langle \mathbf{S}_j(t) \cdot \mathbf{S}_i(0) \rangle$, for this system using the bosonic mean-field theory. We use the extended BZ of the system and plot $S(\mathbf{q}, \omega)$ along the high-symmetry lines in Fig. 3(b).

V. THERMODYNAMIC PROPERTIES

Capturing finite temperature behavior precisely down to low temperatures is a hard problem, but we obtain qualitative information from bond operator theory. The calculated specific heat (see Appendix C and Refs. [50,61,62] for more details) is presented in Fig. 4 together with the experimental result for the magnetic contribution to specific heat [29]. It shows a broad peak around 22 K and matches the overall behavior of the experimental data. The specific heat shape that was interpreted via the Bonner-Fisher fit for the 1D Heisenberg chain [29] is captured well by our 2D wavefunction. This may be rationalized by the fact [63] that zero-, one- and two-dimensional magnets can all have the same overall shape of specific heat (and magnetic susceptibility). The magnetic entropy calculation further validates the effective spin-1 kagome behavior of the system by approaching $\frac{1}{2} \ln 3$ at high temperature (the factor of 1/2 is due to two spin-1/2 combining to form a spin 1), instead of $\ln 2$ which would be the case for a fully AFM system. The residual entropy comes from the interlocking of the spins across the J_1 bonds at low temperatures.

Our approximate 2D Hamiltonian, however, does not exhibit any magnetic ordering, as indicated in experiments by a distinct peak in susceptibility at 17 K [29]. The onset of a magnetic order can be attributed to additional inter- and intralayer couplings. The interlayer couplings J_6, J_8, J_{18} , and J_{20} are all comparable to the spin gap estimated for the

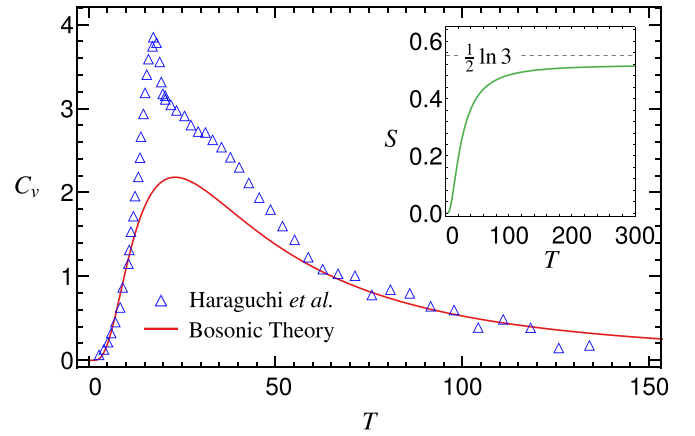


FIG. 4. Thermodynamic properties obtained from bond-operator mean-field theory. Magnetic specific heat $C_{\text{mag}}(T)$ obtained from bond-operator mean-field theory overlaid with the experimental data presented by Haraguchi *et al.* in Ref. [29]. Inset: Magnetic entropy $S_{\text{mag}}(T)$.

approximate 2D Hamiltonian and do not introduce any frustration between the layers. Moreover, J_6 and J_{18} connect the J_4 and J_5 triangles in two neighboring layers. The tendency of the J_4 (strongest interaction in the system) triangles to form a 120° order will also significantly force the formation of a magnetic order on the J_5 triangles across the layers. Therefore, as also seen in other Haldane gapped systems [64,65], these interactions are more than enough to induce a magnetic ordering at 17 K, the inverse of which scales as the logarithm of interlayer couplings, at least, for the unfrustrated case [66]. Another crucial element behind the magnetic ordering might be the strengthening of further-neighbor intralayer couplings upon the lowering of temperature. For instance, in our current estimation, the intralayer second-neighbor interactions in the effective spin-1 kagome picture are found to be 1–3 K (see Appendix A), where a magnetic order can be induced in that system for second-neighbor interactions of strength ~ 10 K [44]. Therefore, the magnetic ordering at low-T might also be indicative of small structural changes upon temperature lowering. Interestingly, an anomalous behavior of the specific heat, however, was also seen in our approximate DMRG-based calculations (see Appendix B) which is related to the thermal activation of other excited states which live above the triplet excitations [67,68].

VI. CONCLUSIONS

We have determined the Heisenberg Hamiltonian for bluebellite by density functional theory (DFT) energy mapping and found that two of the five dominant couplings (all intralayer) in the slightly distorted maple leaf lattice are ferromagnetic. Based on the DMRG result indicating that the second largest antiferromagnetic exchange leads to strong antiferromagnetic spin correlations, we have developed a bond operator mean-field theory for bluebellite which gives us access to thermodynamic properties. Our calculated specific heat does not show a sharp ordering peak as the ground state for the 2D approximate Hamiltonian is magnetically

disordered. However, there is excellent agreement in the overall shape of the specific heat, and we obtain the apparent Bonner-Fisher-type curve, which was interpreted as 1D physics [29], from our fully 2D maple leaf Hamiltonian. Furthermore, focusing on strong ferromagnetic spin correlations in our calculations, we find that bluebellite realizes an effective spin-1 breathing kagome system. We predict both static and dynamic spin structure factors and understand them based on the classical order of the effective kagome model. As the maple leaf Hamiltonian and the effective spin-1 kagome model are determined from a room temperature crystal structure, they are both expected to show a $1/3$ magnetization plateau which, however, was not observed in the $T = 4.2$ K magnetization process [29]. Therefore, it will be very interesting future work to experimentally determine a low-temperature crystal structure of bluebellite and to study its Hamiltonian.

Note added. Recently, one of us has predicted a close connection between bluebellite and quantum spin liquid in maple leaf systems [69,70].

ACKNOWLEDGMENTS

We thank Y. Haraguchi for allowing us to replot the magnetic specific heat. We thank F. Mila for useful discussions. The work in Würzburg is supported by the Deutsche Forschungsgemeinschaft (DFG, German Research Foundation) through Project ID No. 258499086-SFB 1170 and the Würzburg-Dresden Cluster of Excellence on Complexity and Topology in Quantum Matter – ct.qmat Project ID No. 390858490-EXC 2147. R.T. and H.O.J. thank IIT Madras for a visiting faculty fellow position under the IoE program which facilitated the completion of this research work. The work of Y.I. was performed in part at the Aspen Center for Physics, which is supported by National Science Foundation Grant No. PHY-2210452. The participation of Y.I. at the Aspen Center for Physics was supported by a grant from the Simons Foundation (Grant No. 1161654, Troyer). The research of Y.I. was supported, in part, by the National Science Foundation under Grant No. NSF PHY-2309135. Y.I. acknowledges support from the ICTP through the Associates Programme and from the Simons Foundation through Grant No. 284558FY19, IIT Madras through the Institute of Eminence (IoE) program for establishing QuCenDiEM (Project No. SP22231244CPETWOQCDHOC), and the International Centre for Theoretical Sciences (ICTS), Bengaluru, India during a visit for participating in the program Frustrated Metals and Insulators (Code No. ICTS/frumi2022/9). Y.I. acknowledges the use of the computing resources at HPCE, IIT Madras.

APPENDIX A: DETAILS OF ELECTRONIC STRUCTURE CALCULATIONS AND ENERGY MAPPING

Preparation of crystal structure. The crystal structure of bluebellite $\text{Cu}_6\text{IO}_3(\text{OH})_{10}\text{Cl}$ has been determined from mineral samples [26] and from synthetic polycrystals [29]. In the latter case, hydrogen positions were not determined. As the magnetic measurements were performed for synthetic bluebellite, it is necessary to prepare the crystal structure for electronic structure calculations and energy mapping by

adding and optimizing hydrogen positions. Furthermore, Cl, O2, and H2 all have coordinates $(0,0,z)$, restricting their position by symmetry to an axis, and H2 needs to be placed between Cl and O2, in accordance with the Mills *et al.* structure [26]. At a distance $d_{\text{Cl-O2}} = 2.205 \text{ \AA}$, there is insufficient space for an O2-H2 bond and a Cl-H hydrogen bond. Therefore, Cl and O2 positions need to be optimized as well. For consistency, we optimize all O positions as well. The resulting structure is given in Table II.

DFT energy mapping. We determine the Heisenberg Hamiltonian parameters of bluebellite by DFT energy mapping. For this purpose, we create a $\sqrt{2} \times \sqrt{2} \times 1$ supercell of the structure given in Table II with 12 symmetry inequivalent Cu^{2+} sites. This provides 948 distinct energies of spin configurations and allows us to resolve the first 20 nearest-neighbor exchange paths which we name J_1 to J_{20} . We calculate 40 of these energies for five different values of the on-site interaction strength U ; this provides us the five sets of exchange interactions given in Table I with statistical errors given in brackets. Slight extrapolation leads to the line in boldface that matches the experimental value of the Curie-Weiss temperature which we calculate according to

$$\begin{aligned} \theta_{\text{CW}} = & -\frac{1}{3}S(S+1)(J_1 + J_2 + J_3 + J_4 + J_5 + J_6 + J_7 \\ & + J_8 + J_9 + J_{10} + J_{11} + J_{12} + J_{13} + J_{14} \\ & + J_{15} + J_{16} + J_{17} + J_{18} + J_{19} + J_{20}). \end{aligned} \quad (\text{A1})$$

The couplings J_1 to J_5 are the nearest-neighbor couplings making up the maple leaf lattice; they are by far the largest couplings in the model, and they are the main focus of our analysis. Couplings J_6 to J_{10} [for an illustration see Fig. 1(b)] as well as J_{15} , J_{16} and J_{18} to J_{20} are interlayer couplings. They are at most 10% of the dominant coupling J_4 . The couplings J_{11} to J_{14} and J_{17} are second-neighbor couplings in the maple leaf lattice. They are at most 4% of the dominant coupling J_4 .

Effective model. As explained above, the large ferromagnetic J_1 bonds of bluebellite lead to an effective spin-1 breathing kagome lattice behavior. In order to determine the exchange interactions of this effective model, we performed energy mapping in a $3 \times 1 \times 1$ supercell with 18 Cu sites where we constrained moments adjacent to the J_1 bond to be parallel. In this way, we determine the effective exchange interaction for the spin-1 breathing kagome lattice. As shown in Fig. 5, we perform the energy mapping for five different U values. We use the same U value that is relevant for the original maple leaf lattice (see Fig. 1) to determine the effective Hamiltonian parameters. The result is $J_{\text{eff}} = 49(2) \text{ K}$, $J'_{\text{eff}} = 18(2) \text{ K}$, $J_{1,\text{eff}} = -2(3) \text{ K}$, $J_{3,\text{eff}} = 1(2) \text{ K}$, $J_{2,\text{eff}} = -3(2) \text{ K}$, $J'_{2,\text{eff}} = 1(2) \text{ K}$. Due to the error bars, not so much information about the subleading couplings can be obtained. It is clear that the effective kagome lattice has only very small interlayer couplings $J_{i,\text{eff}}^\perp$. The in-plane second-neighbor couplings on average appear to be slightly ferromagnetic.

APPENDIX B: DMRG METHODS AND RESULTS

The ground state energy of the bluebellite Hamiltonian, introduced above, is calculated via DMRG using the ITENSOR [49] package. For the calculations, we use three different sized spin tubes with $N = 2, 3$, and 4 unit cells along the circumference of the tube. Along the length of the tube we

TABLE I. Exchange interactions of bluebellite obtained by DFT energy mapping as described above. The line in boldface corresponds to the set of couplings that match the experimental Curie-Weiss temperature [29]. The distances d given in the last line are the Cu-Cu distances that identify the exchange paths.

U eV	J_1 (K)	J_2 (K)	J_3 (K)	J_4 (K)	J_5 (K)	J_6 (K)	J_7 (K)	J_8 (K)	J_9 (K)	J_{10} (K)
3.9	-120.8(1.3)	88.6(1.2)	-93.7(1.0)	147.6(1.3)	61.3(7)	15.4(1.4)	-1.6(7)	14.7(1.9)	-0.4(1.3)	-12.3(6)
4	-120.1(1.3)	84.0(1.2)	-92.1(1.0)	145.9(1.3)	60.2(7)	15.0(1.4)	-1.5(7)	14.4(1.9)	-0.1(1.3)	-12.1(6)
5	-112.0(9)	41.2(8)	-76.2(7)	127.5(9)	49.9(5)	11.6(9)	-0.4(5)	10.7(1.2)	1.8(8)	-10.2(4)
6	-103.6(6)	11.2(5)	-63.9(5)	111.3(6)	42.0(3)	8.9(7)	0.2(3)	8.0(8)	2.6(6)	-8.6(3)
7	-95.2(4)	-10.0(4)	-54.0(4)	97.1(4)	35.9(2)	6.9(5)	0.6(2)	6.0(6)	2.8(4)	-7.3(2)
8	-87.1(3)	-24.9(3)	-46.1(3)	84.5(3)	31.0(2)	5.3(4)	0.7(2)	4.5(5)	2.7(3)	-6.1(2)
d (Å)	2.992	3.000	3.165	3.287	3.453	4.567	4.673	4.674	4.700	4.968

U eV	J_{11} (K)	J_{12} (K)	J_{13} (K)	J_{14} (K)	J_{15} (K)	J_{16} (K)	J_{17} (K)	J_{18} (K)	J_{19} (K)	J_{20}	θ_{CW} (K)
3.9	-3.8(7)	6.4(1.1)	-0.6(1.2)	3.0(2.0)	-1.4(1.3)	-5.4(7)	-5.1(6)	14.6(6)	6.9(1.9)	12.6(1.1)	-34.7
4	-3.8(7)	6.3(1.1)	-0.7(1.2)	3.0(2.0)	-1.3(1.3)	-5.3(7)	-5.0(6)	14.4(6)	6.8(1.9)	12.4(1.1)	-33.2
5	-3.5(5)	4.9(7)	-1.1(8)	3.0(1.3)	-0.7(9)	-4.1(4)	-3.8(4)	12.5(4)	5.4(1.2)	10.4(7)	-19.3
6	-3.0(3)	3.8(5)	-1.1(6)	2.8(9)	-0.3(6)	-3.2(3)	-2.9(3)	10.7(3)	4.3(8)	8.8(5)	-9.2
7	-2.4(2)	3.0(4)	-1.0(4)	2.5(6)	-0.1(4)	-2.5(2)	-2.1(2)	9.2(2)	3.4(6)	7.4(4)	-1.8
8	-1.9(2)	2.4(3)	-0.8(3)	2.2(5)	0.0(3)	-1.9(2)	-1.6(2)	7.8(2)	2.8(5)	6.2(3)	3.5
d (Å)	5.161	5.434	5.444	5.480	5.691	5.707	5.715	5.725	5.877	5.902	

always take $2N$ unit cells. Thus we do our calculations on $L = 2N^2 = 48, 108, 192$ site clusters. For $L = 48$ and 108 , we perform 30 sweeps with a maximum bond dimension 2048. For $L = 192$ the number of sweeps was reduced to 24. Figures 6(a) and 6(b) shows the scaling of ground state energy and spin-gap. We calculate the spin-spin correlations, $\langle \mathbf{S}_i \cdot \mathbf{S}_j \rangle$, for all nearest-neighbor spin pairs \mathbf{S}_i and \mathbf{S}_j , and find strong singlet formation on the AFM J_2 bonds. Figure 6(c) shows an example at the center of a 108-site cluster. This propensity to form dimers on the J_2 bonds is indicative of a VBS ground state. We perform a linear fitting of the energies to obtain a finite size scaling. The spin-spin correlations from two central sites are shown in Fig. 7(b). A fast decay of the long range spin-spin correlations is apparent there.

Next, to access the thermodynamic properties of the system, we calculate the magnetic specific heat by using the

TABLE II. Crystal structure of bluebellite $\text{Cu}_6\text{IO}_3(\text{OH})_{10}\text{Cl}$ with DFT optimized Cl, O and H positions. The lattice parameters of space group $R\bar{3}$ (No. 146) were kept fixed at experimental values $a = 8.3056$ Å and $c = 13.2194$ Å [29].

Atom	x	y	z
Cu1	0.4578	0.3867	0.2901
Cu2	0.0261	0.2404	0.2747
I	0.0000	0.0000	0.6050
O1	-0.244716	-0.154414	-0.120656
O2	0.000000	0.000000	0.249551
O3	0.190821	0.445737	0.171976
O4	-0.444508	-0.062377	0.031739
O5	0.412671	0.135042	0.022041
Cl	0.000000	0.000000	0.049719
H1	-0.260301	-0.167341	-0.197392
H2	0.000000	0.000000	0.172600
H3	-0.114255	-0.306030	-0.254043
H4	-0.454172	-0.185148	0.109447

fundamental relation

$$C_{\text{mag}} \propto \frac{1}{LT^2} [\langle \hat{H}^2 \rangle_{th} - \langle \hat{H} \rangle_{th}^2], \quad (\text{B1})$$

where, T is the temperature of the system and $\langle \hat{Q} \rangle$ is the thermal average of an observable \hat{Q} , i.e.,

$$\langle \hat{Q} \rangle_{th} = \frac{\sum_j \exp(-\beta E_j) \langle j | \hat{Q} | j \rangle}{\sum_j \exp(-\beta E_j)},$$

where β is the inverse temperature. This relation is easily derivable by taking the second derivative of the partition function

$$Z(\beta) = \sum_j \exp(-\beta E_j),$$

where the j sum runs over all the eigenenergies of the system. For practical calculations, we have to restrict ourselves to a finite number of lowest lying states $|j\rangle$ and their energies E_j known from DMRG. The corresponding expectation values $\langle j | \hat{H} | j \rangle$ and $\langle j | \hat{H}^2 | j \rangle$ are E_j and E_j^2 , respectively. For this part of the calculation we choose the 48 site cluster. We perform 24 sweeps with a maximum bond dimension of 512 and calculate the energies (E_j) of 481 lowest lying states. We estimate that for a L site cluster there will be $L/2$ strong singlets forming on the J_2 bonds. Each such singlet would have three excited triplet states. Therefore, we need more than $3L/2$ excited states to capture the finite temperature physics which will be missed by the bond-operator calculations. Thus it is an extremely costly calculation and also prone to numerical errors, and thus we only perform it on a small cluster to get an idea of the thermodynamic properties of the system which we show in Fig. 7(c). We see an anomalous behavior occurring at ~ 10 K which becomes exceedingly pronounced with increasing number of excited states considered. We believe this comes from the thermal activation of the excited states that live above the triplets. This might also have a connection to the anomalous behavior seen in the experiments at 17 K.

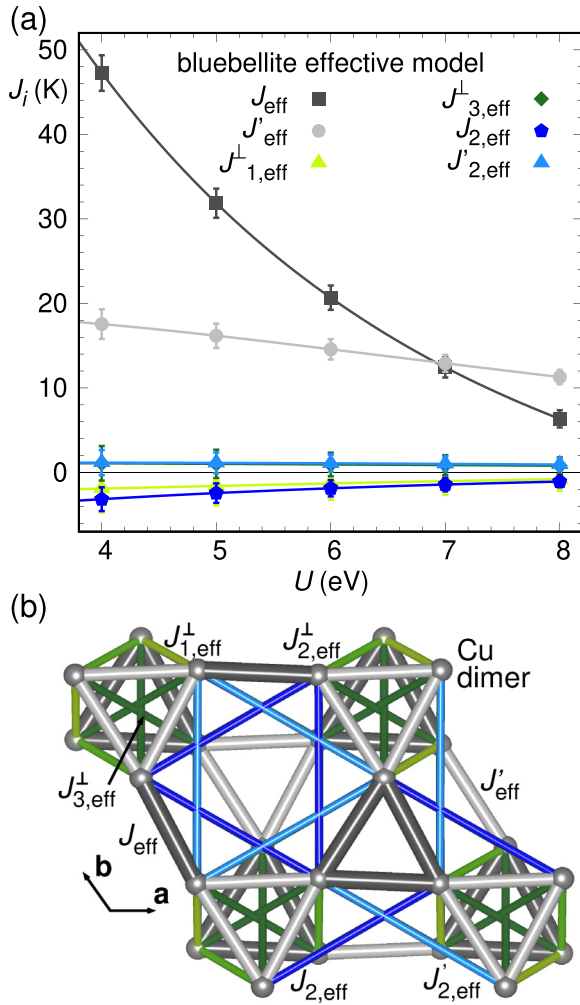


FIG. 5. Energy mapping calculation for the effective spin-1 kagome lattice Hamiltonian. (a) Exchange interactions for five different values of on-site interaction U at fixed Hund's rule coupling strength J_H . (b) Exchange paths of the effective $S = 1$ lattice of bluebellite. Balls represent the Cu dimers of bluebellite with the strongest ferromagnetic coupling. J_{eff} and J'_{eff} correspond to small and large triangles in the breathing kagome network. Couplings marked " \perp " indicate interlayer couplings.

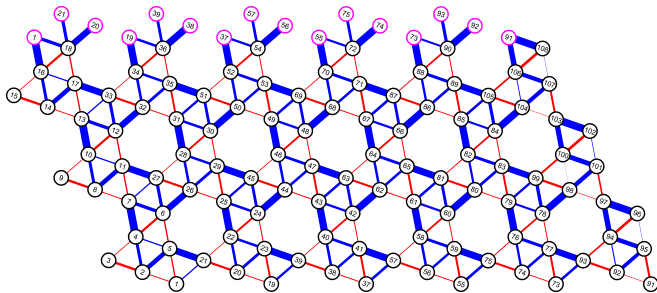


FIG. 6. Spin-spin correlations for all nearest-neighbor bonds obtained from DMRG on a 108 site maple leaf cluster. The thickness of the bonds indicates the strength of the correlation and the color red (blue) indicates positive (negative) correlation. Note the clear dimerization in the ground state.

APPENDIX C: DETAILS OF BOND-OPERATOR MEAN-FIELD THEORY

Based on our findings from the DMRG calculations of the Hamiltonian for bluebellite, we now develop an effective low-energy bosonic theory for various reasons. First we want to obtain a better understanding of the system at the thermodynamic limit. Secondly, such an approximate theory allows us to calculate static and dynamic spin structure factors of the system very easily. Additionally, we can gain some insight into the thermodynamic properties of the system as well.

Upon carefully observing the NN spin-spin correlations obtained from DMRG (see Fig. 1), we propose that a minimal low-energy physics of the system can be well described by assuming that the ground state of the system is a dimerized singlet with strong singlet weights on the J_2 bonds. To understand the effective low-energy physics of the system, we start with a $J_2 - J_3$ hexagon as our unit cell, and only consider the three J_2 bonds as our elementary block, $\begin{smallmatrix} \circ & \circ \\ \circ & \circ \end{smallmatrix}$, described by the Hamiltonian

$$\mathcal{H}_{\begin{smallmatrix} \circ & \circ \\ \circ & \circ \end{smallmatrix}} = J_2 \sum_{b=1,2,3} \left(\vec{S}_{2b-1} \cdot \vec{S}_{2b} \right) \quad (\text{C1})$$

$$= J_2 (\vec{S}_1 \cdot \vec{S}_2 + \vec{S}_3 \cdot \vec{S}_4 + \vec{S}_5 \cdot \vec{S}_6), \quad (\text{C2})$$

where $b = 1, 2, 3$ is the bond index (see Fig. 8). The ground state of this Hamiltonian is a product state of singlets forming on the 1-2, 3-4, and 5-6 spin pairs, which allows us to use the bond-operator formalism [43] to represent the spin operators as

$$S_{2b-1}^{\alpha} = -\frac{1}{2} (\hat{s}_b^{\dagger} \hat{t}_b^{\alpha \dagger} + \hat{s}_b^{\dagger} \hat{t}_b^{\alpha}), \quad (\text{C3a})$$

$$S_{2b}^{\alpha} = \frac{1}{2} (\hat{s}_b \hat{t}_b^{\alpha \dagger} + \hat{s}_b \hat{t}_b^{\alpha}). \quad (\text{C3b})$$

In writing the above representation, one makes use of the basis of the singlet, $|s_b\rangle$, and three triplets, $|t_b^{\pm 1,0}\rangle$, defined on the bond b . On a Fock space with vacuum, $|\emptyset\rangle_b$, the singlet and the triplet operators are defined as

$$|s_b\rangle = \hat{s}_b^{\dagger} |\emptyset\rangle_b, \quad (\text{C4a})$$

$$|t_b^m\rangle = \hat{t}_b^{m\dagger} |\emptyset\rangle_b, \quad (\text{C4b})$$

with \hat{s}_b and \hat{t}_b^m being bosonic operators. A boson number constraint

$$\hat{s}_b^{\dagger} \hat{s}_b + \sum_{m=-1,0,1} \hat{t}_b^{m\dagger} \hat{t}_b^m = 1 \quad (\text{C5})$$

must also be satisfied on every bond. In terms of the singlet and the triplet operators defined above $\mathcal{H}_{\begin{smallmatrix} \circ & \circ \\ \circ & \circ \end{smallmatrix}}$ reads as

$$\mathcal{H}_{\begin{smallmatrix} \circ & \circ \\ \circ & \circ \end{smallmatrix}} = -\frac{3}{4} J_2 \sum_b \hat{s}_b^{\dagger} \hat{s}_b + \frac{1}{4} J_2 \sum_b \sum_{\alpha=x,y,z} \hat{t}_b^{\alpha \dagger} \hat{t}_b^{\alpha} \quad (\text{C6})$$

where

$$\hat{t}_b^{x\dagger} = \frac{1}{\sqrt{2}} (\hat{t}_b^{-1\dagger} - \hat{t}_b^{1\dagger}), \quad (\text{C7a})$$

$$\hat{t}_b^{y\dagger} = \frac{i}{\sqrt{2}} (\hat{t}_b^{-1\dagger} + \hat{t}_b^{1\dagger}), \quad (\text{C7b})$$

$$\hat{t}_b^{z\dagger} = \hat{t}_b^{0\dagger}. \quad (\text{C7c})$$

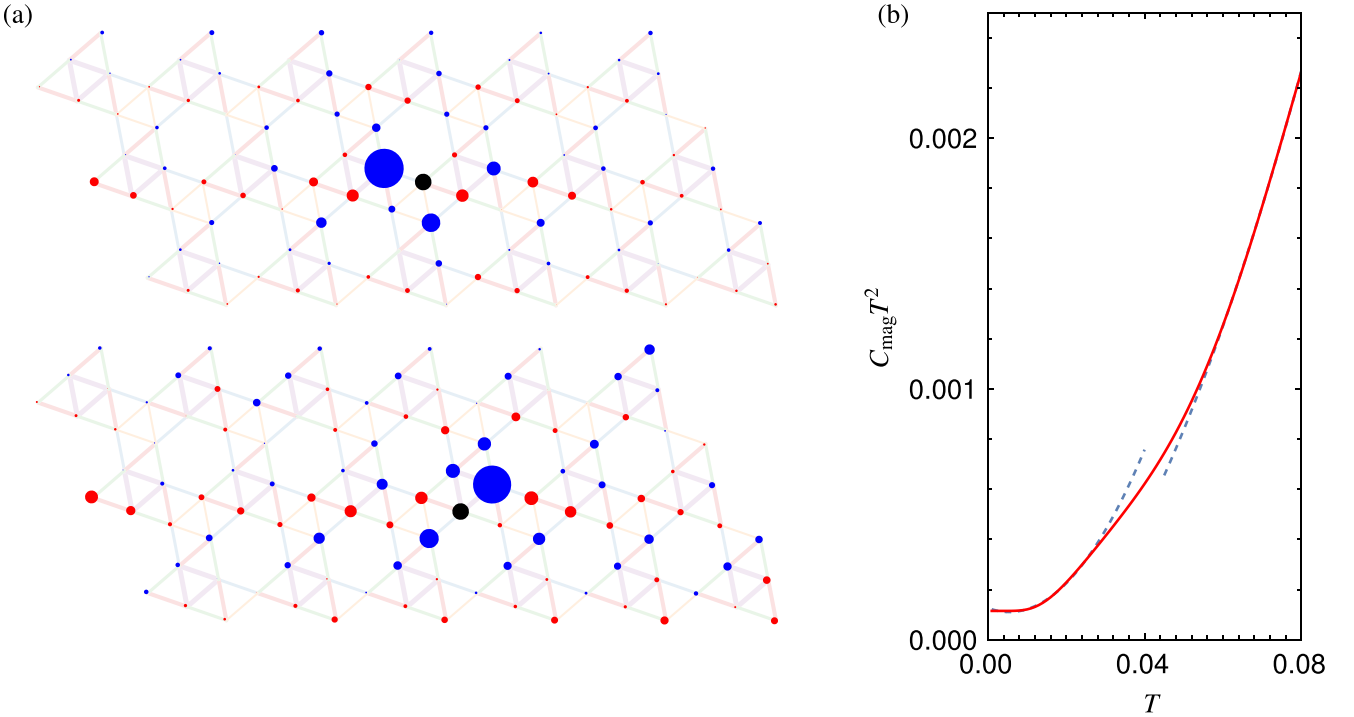


FIG. 7. (a) The spin-spin correlation $\langle \vec{S}_j \cdot \vec{S}_r \rangle$ obtained from DMRG on a 108 site maple leaf cluster. \vec{S}_r is our reference spin which is marked in black. For the top panel we set $r = 63$ and for the bottom panel $r = 62$. The radius of the disks indicates the strength of the correlation and the color red (blue) indicates positive (negative) correlation. In both cases we see that in the bulk the spin-spin correlation decays very quickly, signaling a spin disordered ground state. (b) The $C_{\text{mag}} T^2$ vs T calculated via DMRG on a 48-site cluster. The calculations are done with 24 sweeps with a maximum bond dimension of 1024. Apart from the ground state, we also calculate 480 excited states to calculate the finite temperature properties. The dashed line is a guide for the eye. One can see an anomalous behavior occurring at $\sim 0.04 \tilde{J} = 10$ K which might be seen in the experiments.

Next, we rewrite our full Hamiltonian and recast it in terms of the “coordinate” operator

$$\hat{Q}_b^\alpha = \frac{1}{\sqrt{2}}(\hat{t}_i^{\alpha\dagger} + \hat{t}_i^\alpha) \quad (\text{C8})$$

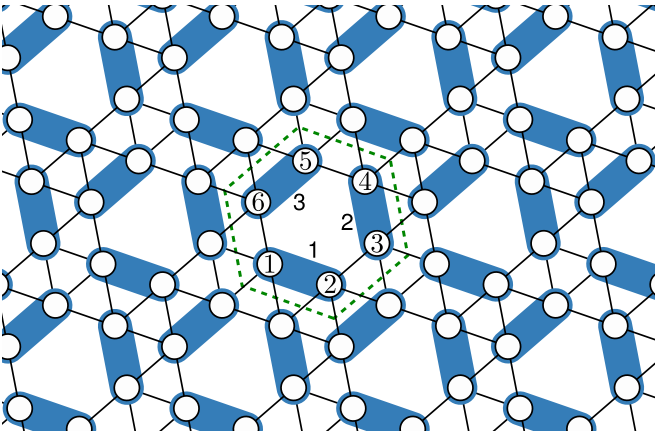


FIG. 8. The singlet product state used in our bond-operator mean-field calculation. The singlets are forming on the J_2 bonds. We use the dashed green hexagon as our unit cell, which contains three symmetry related dimers. The indexing of the bonds and the sites in the unit cell are also marked.

and its conjugate momentum operator

$$\hat{P}_b^\alpha = \frac{i}{\sqrt{2}}(\hat{t}_i^{\alpha\dagger} - \hat{t}_i^\alpha). \quad (\text{C9})$$

Thus, the final form of the full Hamiltonian, \mathcal{H} , on N_{uc} unit cells reads as

$$\mathcal{H} \approx \mathcal{H}_{\text{MF}} = e_0 N_{\text{uc}} + \frac{1}{2} \sum_{\mathbf{k}} \sum_{\alpha} [\lambda \hat{\mathbf{P}}_{\mathbf{k}}^{\alpha\dagger} \hat{\mathbf{P}}_{\mathbf{k}}^{\alpha} + \hat{\mathbf{Q}}_{\mathbf{k}}^{\alpha\dagger} \mathcal{V}_{\mathbf{k}}^{\alpha} \hat{\mathbf{Q}}_{\mathbf{k}}^{\alpha}]. \quad (\text{C10})$$

Here, $e_0 = -3J_2 \bar{s}^2 + \frac{3}{4}J_2 + 3\lambda \bar{s}^2 - \frac{15}{2}\lambda$, with \bar{s} being the mean singlet amplitude on all the J_2 bonds. λ is the Lagrange multiplier used to satisfy the boson number constraint in (C5) on average.

$$\hat{\mathbf{P}}_{\mathbf{k}}^{\alpha\dagger} = [\hat{P}_{1\mathbf{k}}^{\alpha\dagger} \hat{P}_{2\mathbf{k}}^{\alpha\dagger} \hat{P}_{3\mathbf{k}}^{\alpha\dagger}], \quad (\text{C11})$$

$$\hat{\mathbf{Q}}_{\mathbf{k}}^{\alpha\dagger} = [\hat{Q}_{1\mathbf{k}}^{\alpha\dagger} \hat{Q}_{2\mathbf{k}}^{\alpha\dagger} \hat{Q}_{3\mathbf{k}}^{\alpha\dagger}], \quad (\text{C12})$$

and

$$\mathcal{V}_{\mathbf{k}}^{\alpha} = \begin{bmatrix} \lambda & \eta_{12} & \eta_{31}^* \\ \eta_{12}^* & \lambda & \eta_{23} \\ \eta_{31} & \eta_{23}^* & \lambda \end{bmatrix} \quad (\text{C13})$$

with

$$\eta_{12} = \frac{\bar{s}^2}{2} [-J_3 + (J_5 - J_1)e^{i\mathbf{k} \cdot \mathbf{a}_2} + J_4 e^{i\mathbf{k} \cdot \mathbf{a}_1}], \quad (\text{C14a})$$

$$\eta_{23} = \frac{\bar{s}^2}{2}[-J_3 + (J_5 - J_1)e^{-ik \cdot \mathbf{a}_1} + J_4 e^{-ik \cdot (\mathbf{a}_1 - \mathbf{a}_2)}], \quad (\text{C14b})$$

$$\eta_{31} = \frac{\bar{s}^2}{2}[-J_3 + (J_5 - J_1)e^{ik \cdot (\mathbf{a}_1 - \mathbf{a}_2)} + J_4 e^{-ik \cdot \mathbf{a}_2}] \quad (\text{C14c})$$

(the lattice vectors $\mathbf{a}_1 = \sqrt{7}/2(\hat{x} + \sqrt{3}\hat{y})$ and $\mathbf{a}_2 = \sqrt{7}\hat{x}$). Moreover, $\hat{P}_{bk}^{\alpha\dagger}$'s and $\hat{Q}_{bk}^{\alpha\dagger}$'s are the Fourier components of $\hat{P}_b^{\alpha\dagger}(\mathbf{r})$'s and $\hat{Q}_b^{\alpha\dagger}(\mathbf{r})$'s, respectively, i.e., $\hat{P}_{bk}^{\alpha\dagger} = 1/\sqrt{N_{uc}} \sum_{\mathbf{r}} e^{ik \cdot \mathbf{r}} \hat{P}_b^{\alpha\dagger}(\mathbf{r})$ and $\hat{Q}_{bk}^{\alpha\dagger} = 1/\sqrt{N_{uc}} \sum_{\mathbf{r}} e^{ik \cdot \mathbf{r}} \hat{Q}_b^{\alpha\dagger}(\mathbf{r})$.

\mathcal{H}_{MF} now is a problem of three coupled differential equations, which one diagonalizes to obtain

$$\mathcal{H}_{MF} = e_0 N_{uc} + \sum_m \sum_{\mathbf{k}} \sum_{\alpha} \omega_{\mathbf{k},m}^{\alpha} \left(\gamma_{\mathbf{k},m}^{\alpha\dagger} \gamma_{\mathbf{k},m}^{\alpha} + \frac{1}{2} \right), \quad (\text{C15})$$

where $\gamma_{\mathbf{k},m}^{\alpha}$ are renormalized triplon operators, and

$$\omega_{\mathbf{k},m}^{\alpha} = \sqrt{\lambda \left(\lambda - \frac{1}{2} \bar{s}^2 \xi_{\mathbf{k},m}^{\alpha} \right)} \quad (\text{C16})$$

with

$$\xi_{\mathbf{k},m}^{\alpha} = 2\sqrt{-\frac{p_{\mathbf{k}}}{3}} \cos \left[\frac{1}{3} \cos^{-1} \left(\frac{3q_{\mathbf{k}}}{2p_{\mathbf{k}}} \sqrt{-\frac{3}{p_{\mathbf{k}}}} - \frac{2\pi}{3} m \right) \right], \quad (\text{C17})$$

and

$$p_{\mathbf{k}} = -(|\eta_{12}|^2 + |\eta_{23}|^2 + |\eta_{31}|^2), \quad (\text{C18})$$

$$q_{\mathbf{k}} = 2\text{Re}(\eta_{12}\eta_{23}\eta_{31}). \quad (\text{C19})$$

The ground state of the system is given by the vacuum of the quasiparticles, $\gamma_{\mathbf{k},m}^{\alpha}$, i.e., the ground state energy per site of the system is given by

$$e_g = \frac{e_0}{6} + \frac{1}{12N_{uc}} \sum_m \sum_{\mathbf{k}} \sum_{\alpha} \omega_{\mathbf{k},m}^{\alpha}. \quad (\text{C20})$$

The unknown mean-field parameters, λ and \bar{s}^2 are determined by minimizing e_g , which leads to the following self-consistent equations:

$$\lambda = J_2 + \frac{1}{12N_{uc}} \sum_m \sum_{\mathbf{k}} \sum_{\alpha} \frac{\lambda \xi_{\mathbf{k},m}^{\alpha}}{2\omega_{\mathbf{k},m}^{\alpha}}, \quad (\text{C21a})$$

$$\bar{s}^2 = \frac{5}{2} - \frac{1}{12N_{uc}} \sum_m \sum_{\mathbf{k}} \sum_{\alpha} \frac{4\lambda - \bar{s}^2 \xi_{\mathbf{k},m}^{\alpha}}{2\omega_{\mathbf{k},m}^{\alpha}}. \quad (\text{C21b})$$

To access finite temperature properties from the bond-operator mean-field theory we employ the methodology used by Normand *et al.* [50]. First of all, a full thermal occupation function of hard-core bosons is impossible to obtain because of the exclusion constraint of Eq. (C5). It can, however, be approximated via a statistical reweighting of the free-boson numbers [61], i.e., suppressing the magnon density of states for all magnon sectors, the more magnons in a sector, the stronger the suppression. This leads to the effective

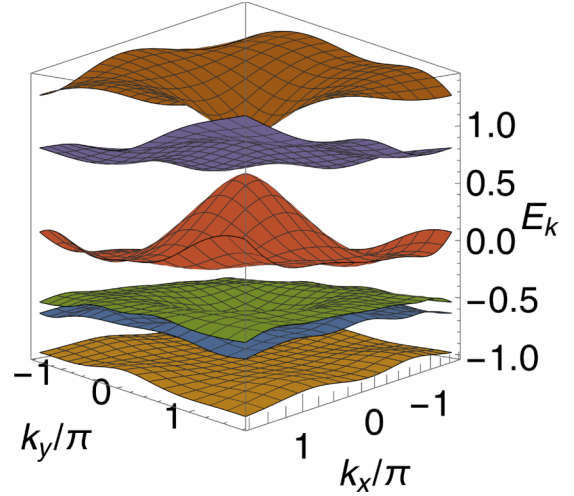


FIG. 9. Luttinger-Tisza band-structure of the full bluebellite model Hamiltonian. The lowest band has a width of 4% of \bar{J} with soft minima along the Γ - M direction within an almost flat area around the origin in reciprocal space.

single-dimer free energy

$$f = -\frac{1}{\beta} \ln \left[1 + \sum_{m,\alpha} z_{m,\alpha}(\beta) \right], \quad (\text{C22})$$

where

$$z_{m,\alpha}(\beta) = \frac{1}{N_{uc}} \sum_{\mathbf{k}} \exp(-\beta \omega_{\mathbf{k},m}^{\alpha})$$

is the partition function of the triplet t_m^{α} . The effective statistics obtained from such a statistical ansatz are given by

$$n(\omega_{\mathbf{k},m}^{\alpha}, \beta) = \frac{\exp(-\beta \omega_{\mathbf{k},m}^{\alpha})}{1 + \sum_{m,\alpha} z_{m,\alpha}(\beta)}, \quad (\text{C23})$$

where β is the inverse temperature [62]. The magnetic specific heat, hereafter, is easily derived by taking a second derivative of the free-energy with respect to temperature. The magnetic specific heat thus obtained reads as

$$C_{\text{mag}}(\beta) = \sum_{m,\mathbf{k},\alpha} \left[\frac{(\beta \omega_{\mathbf{k},m}^{\alpha})^2 \exp(-\beta \omega_{\mathbf{k},m}^{\alpha})}{1 + \frac{1}{N_{uc}} \sum_{m,\mathbf{k},\alpha} \exp(-\beta \omega_{\mathbf{k},m}^{\alpha})} - \left\{ \frac{\beta \omega_{\mathbf{k},m}^{\alpha} \exp(-\beta \omega_{\mathbf{k},m}^{\alpha})}{1 + \frac{1}{N_{uc}} \sum_{m,\mathbf{k},\alpha} \exp(-\beta \omega_{\mathbf{k},m}^{\alpha})} \right\}^2 \right]. \quad (\text{C24})$$

The results obtained from the finite temperature calculations are depicted in Fig. 3.

APPENDIX D: LUTTINGER-TISZA ANALYSIS OF THE BLUEBELLITE

The full model Hamiltonian of bluebellite is not amenable to a solution in the classical, i.e., $S \rightarrow \infty$ limit, where spin operators are replaced by vector spins. Therefore, we resort to the Luttinger-Tisza approximation [71,72], where the normalization of the spins is enforced only on average, allowing for analytical solution of the model. The corresponding band

structure in Fig. 9 shows a flat lowest band with a bandwidth of 4% of \tilde{J} , and an almost degenerate area around the Γ point, featuring soft minima along the $\Gamma-M$ direction. While in the classical limit, even in the Luttinger-Tisza approximation, this energy landscape implies an ordered ground state, quantum

fluctuations can access these low-lying states by allowing for variations in the spin expectation values. Therefore, the flatness of the lowest Luttinger-Tisza band indicates the probability for the quantum model to avoid long-range order, as we find for bluebellite.

- [1] *Introduction to Frustrated Magnetism: Materials, Experiments, Theory*, edited by C. Lacroix, P. Mendels, and F. Mila (Springer, Berlin, 2011).
- [2] H. T. Diep, *Frustrated Spin Systems* (World Scientific, Singapore, 2012).
- [3] L. Balents, Spin liquids in frustrated magnets, *Nature (London)* **464**, 199 (2010).
- [4] Y. Iqbal, P. Ghosh, R. Narayanan, B. Kumar, J. Reuther, and R. Thomale, Intertwined nematic orders in a frustrated ferromagnet, *Phys. Rev. B* **94**, 224403 (2016).
- [5] J. Richter, J. Schulenburg, and A. Honecker, Quantum magnetism in two dimensions: From semi-classical Néel order to magnetic disorder, in *Quantum Magnetism*, edited by U. Schollwöck, J. Richter, D. J. J. Farnell, and R. F. Bishop (Springer, Berlin, 2004), pp. 85–153.
- [6] H. Lu and H. Kageyama, $\text{PbFePO}_4\text{F}_2$ with a $1/6$ th bond depleted triangular lattice, *Dalton Trans.* **47**, 15303 (2018).
- [7] P. Mendels and A. S. Wills, Kagomé antiferromagnets: Materials vs. spin liquid behaviors, in *Introduction to Frustrated Magnetism: Materials, Experiments, Theory*, edited by C. Lacroix, P. Mendels, and F. Mila (Springer, Berlin, 2011), pp. 207–238.
- [8] D. D. Betts, A new two-dimensional lattice of coordination number five, *Proc. N. S. Inst. Sci.* **40**, 95 (1995).
- [9] D. Schmalfuß, P. Tomczak, J. Schulenburg, and J. Richter, The spin- $\frac{1}{2}$ Heisenberg antiferromagnet on a $\frac{1}{7}$ -depleted triangular lattice: Ground-state properties, *Phys. Rev. B* **65**, 224405 (2002).
- [10] D. J. J. Farnell, R. Darradi, R. Schmidt, and J. Richter, Spin-half Heisenberg antiferromagnet on two archimedean lattices: From the bounce lattice to the maple-leaf lattice and beyond, *Phys. Rev. B* **84**, 104406 (2011).
- [11] D. J. J. Farnell, O. Götze, J. Richter, R. F. Bishop, and P. H. Y. Li, Quantum $s = \frac{1}{2}$ antiferromagnets on Archimedean lattices: The route from semiclassical magnetic order to nonmagnetic quantum states, *Phys. Rev. B* **89**, 184407 (2014).
- [12] D. J. J. Farnell, O. Götze, J. Schulenburg, R. Zinke, R. F. Bishop, and P. H. Y. Li, Interplay between lattice topology, frustration, and spin quantum number in quantum antiferromagnets on Archimedean lattices, *Phys. Rev. B* **98**, 224402 (2018).
- [13] L. Gresista, C. Hickey, S. Trebst, and Y. Iqbal, Candidate quantum disordered intermediate phase in the Heisenberg antiferromagnet on the maple-leaf lattice, *Phys. Rev. B* **108**, L241116 (2023).
- [14] J. Beck, J. Bodky, J. Motruk, T. Müller, R. Thomale, and P. Ghosh, Phase diagram of the $J-J_d$ Heisenberg model on the maple-leaf lattice: Neural networks and density matrix renormalization group, *Phys. Rev. B* **109**, 184422 (2024).
- [15] P. Ghosh, T. Müller, and R. Thomale, Another exact ground state of a two-dimensional quantum antiferromagnet, *Phys. Rev. B* **105**, L180412 (2022).
- [16] B. S. Shastry and B. Sutherland, Exact ground state of a quantum mechanical antiferromagnet, *Physica B+C* **108**, 1069 (1981).
- [17] J. L. Jiménez, S. P. G. Crone, E. Fogh, M. E. Zayed, R. Lortz, E. Pomjakushina, K. Conder, A. M. Läuchli, L. Weber, S. Wessel, A. Honecker, B. Normand, C. Rüegg, P. Corboz, H. M. Rønnow, and F. Mila, A quantum magnetic analogue to the critical point of water, *Nature (London)* **592**, 370 (2021).
- [18] Z. Shi, S. Dissanayake, P. Corboz, W. Steinhardt, D. Graf, D. M. Silevitch, H. A. Dabkowska, T. F. Rosenbaum, F. Mila, and S. Haravifard, Discovery of quantum phases in the Shastry-Sutherland compound $\text{SrCu}_2(\text{BO}_3)_2$ under extreme conditions of field and pressure, *Nat. Commun.* **13**, 2301 (2022).
- [19] J. Y. Lee, Y.-Z. You, S. Sachdev, and A. Vishwanath, Signatures of a deconfined phase transition on the Shastry-Sutherland lattice: Applications to quantum critical $\text{SrCu}_2(\text{BO}_3)_2$, *Phys. Rev. X* **9**, 041037 (2019).
- [20] P. Corboz and F. Mila, Crystals of bound states in the magnetization plateaus of the Shastry-Sutherland model, *Phys. Rev. Lett.* **112**, 147203 (2014).
- [21] S. Miyahara and K. Ueda, Exact dimer ground state of the two dimensional Heisenberg spin system $\text{SrCu}_2(\text{BO}_3)_2$, *Phys. Rev. Lett.* **82**, 3701 (1999).
- [22] M. Norman, Copper tellurium oxides – a playground for magnetism, *J. Magn. Magn. Mater.* **452**, 507 (2018).
- [23] D. Inosov, Quantum magnetism in minerals, *Adv. Phys.* **67**, 149 (2018).
- [24] F. C. Hawthorne, M. Kimata, and R. K. Eby, The crystal structure of spangolite, a complex copper sulfate sheet mineral, *Am. Mineralog.* **78**, 649 (1993).
- [25] F. Olmi, C. Sabelli, and R. Trosti-Ferroni, The crystal structure of sabelliite, *Eur. J. Mineral.* **7**, 1331 (1995).
- [26] S. J. Mills, A. R. Kampf, A. G. Christy, R. M. Housley, G. R. Rossman, R. E. Reynolds, and J. Marty, Bluebellite and mojaveite, two new minerals from the central Mojave Desert, California, USA, *Mineralog. Mag.* **78**, 1325 (2014).
- [27] A. R. Kampf, S. J. Mills, R. M. Housley, and J. Marty, Lead-tellurium oxysalts from Otto Mountain near Baker, California: VIII. Fuettererite, $\text{Pb}_3\text{Cu}^{2+}_6\text{Te}^{6+}_6\text{O}_6(\text{OH})_7\text{Cl}_5$, a new mineral with double spangolite-type sheets, *Am. Mineral.* **98**, 506 (2013).
- [28] T. Fennell, J. O. Piatek, R. A. Stephenson, G. J. Nilsen, and H. M. Rønnow, Spangolite: an $s = 1/2$ maple leaf lattice antiferromagnet? *J. Phys.: Condens. Matter* **23**, 164201 (2011).
- [29] Y. Haraguchi, A. Matsuo, K. Kindo, and Z. Hiroi, Quantum antiferromagnet bluebellite comprising a maple-leaf lattice made of spin- $1/2$ Cu^{2+} ions, *Phys. Rev. B* **104**, 174439 (2021).
- [30] R. Makuta and C. Hotta, Dimensional reduction in quantum spin- $\frac{1}{2}$ system on a $\frac{1}{7}$ -depleted triangular lattice, *Phys. Rev. B* **104**, 224415 (2021).

- [31] H. Jeschke, I. Opahle, H. Kandpal, R. Valentí, H. Das, T. Saha-Dasgupta, O. Janson, H. Rosner, A. Brühl, B. Wolf, M. Lang, J. Richter, S. Hu, X. Wang, R. Peters, T. Pruschke, and A. Honecker, Multistep approach to microscopic models for frustrated quantum magnets: The case of the natural mineral azurite, *Phys. Rev. Lett.* **106**, 217201 (2011).
- [32] H. O. Jeschke, F. Salvat-Pujol, and R. Valentí, First-principles determination of Heisenberg Hamiltonian parameters for the spin- $\frac{1}{2}$ kagome antiferromagnet $\text{ZnCu}_3(\text{OH})_6\text{Cl}_2$, *Phys. Rev. B* **88**, 075106 (2013).
- [33] D. Guterding, R. Valentí, and H. O. Jeschke, Reduction of magnetic interlayer coupling in barlowite through isoelectronic substitution, *Phys. Rev. B* **94**, 125136 (2016).
- [34] O. Janson, S. Furukawa, T. Momoi, P. Sindzingre, J. Richter, and K. Held, Magnetic behavior of volborthite $\text{Cu}_3\text{V}_2\text{O}_7(\text{OH})_2 \cdot 2\text{H}_2\text{O}$ determined by coupled trimers rather than frustrated chains, *Phys. Rev. Lett.* **117**, 037206 (2016).
- [35] Y. Iqbal, H. O. Jeschke, J. Reuther, R. Valentí, I. I. Mazin, M. Greiter, and R. Thomale, Paramagnetism in the kagome compounds $(\text{Zn}, \text{Mg}, \text{Cd})\text{Cu}_3(\text{OH})_6\text{Cl}_2$, *Phys. Rev. B* **92**, 220404(R) (2015).
- [36] Y. Iqbal, T. Müller, K. Riedl, J. Reuther, S. Rachel, R. Valentí, M. J. P. Gingras, R. Thomale, and H. O. Jeschke, Signatures of a gearwheel quantum spin liquid in a spin- $\frac{1}{2}$ pyrochlore molybdate Heisenberg antiferromagnet, *Phys. Rev. Mater.* **1**, 071201(R) (2017).
- [37] Y. Iqbal, T. Müller, H. O. Jeschke, R. Thomale, and J. Reuther, Stability of the spiral spin liquid in MnSc_2S_4 , *Phys. Rev. B* **98**, 064427 (2018).
- [38] P. Ghosh, Y. Iqbal, T. Müller, R. T. Ponnaganti, R. Thomale, R. Narayanan, J. Reuther, M. J. P. Gingras, and H. O. Jeschke, Breathing chromium spinels: a showcase for a variety of pyrochlore Heisenberg Hamiltonians, *npj Quantum Mater.* **4**, 63 (2019).
- [39] S. Chillal, Y. Iqbal, H. O. Jeschke, J. A. Rodriguez-Rivera, R. Bewley, P. Manuel, D. Khalyavin, P. Steffens, R. Thomale, A. T. M. N. Islam, J. Reuther, and B. Lake, Evidence for a three-dimensional quantum spin liquid in $\text{PbCuTe}_2\text{O}_6$, *Nat. Commun.* **11**, 2348 (2020).
- [40] K. Iida, H. K. Yoshida, A. Nakao, H. O. Jeschke, Y. Iqbal, K. Nakajima, S. Ohira-Kawamura, K. Munakata, Y. Inamura, N. Murai, M. Ishikado, R. Kumai, T. Okada, M. Oda, K. Kakurai, and M. Matsuda, $q = 0$ long-range magnetic order in centennialite $\text{CaCu}_3(\text{OD})_6\text{Cl}_2 \cdot 0.6\text{D}_2\text{O}$: A spin- $\frac{1}{2}$ perfect kagome antiferromagnet with $J_1 - J_2 - J_d$, *Phys. Rev. B* **101**, 220408(R) (2020).
- [41] I. Živković, V. Favre, C. Salazar Mejia, H. O. Jeschke, A. Magrez, B. Dabholkar, V. Nocolak, R. S. Freitas, M. Jeong, N. G. Hegde, L. Testa, P. Babkevich, Y. Su, P. Manuel, H. Luetkens, C. Baines, P. J. Baker, J. Wosnitza, O. Zaharko, Y. Iqbal, J. Reuther, and H. M. Rønnow, Magnetic field induced quantum spin liquid in the two coupled trillium lattices of $\text{K}_2\text{Ni}_2(\text{SO}_4)_3$, *Phys. Rev. Lett.* **127**, 157204 (2021).
- [42] S. R. White, Density matrix formulation for quantum renormalization groups, *Phys. Rev. Lett.* **69**, 2863 (1992).
- [43] S. Sachdev and R. N. Bhatt, Bond-operator representation of quantum spins: Mean-field theory of frustrated quantum Heisenberg antiferromagnets, *Phys. Rev. B* **41**, 9323 (1990).
- [44] P. Ghosh, A. K. Verma, and B. Kumar, Plaquette-triplon analysis of magnetic disorder and order in a trimerized spin-1 kagome Heisenberg antiferromagnet, *Phys. Rev. B* **93**, 014427 (2016).
- [45] S. Hara, H. Sato, and Y. Narumi, Exotic magnetism of novel $S = 1$ kagome lattice antiferromagnet $\text{KV}_3\text{Ge}_2\text{O}_9$, *J. Phys. Soc. Jpn.* **81**, 073707 (2012).
- [46] H. Kato, M. Kato, K. Yoshimura, and K. Kosuge, ^{23}Na -NMR study in $\text{NaV}_6\text{O}_{11}$, *J. Phys. Soc. Jpn.* **70**, 1404 (2001).
- [47] N. Wada, T. Kobayashi, H. Yano, T. Okuno, A. Yamaguchi, and K. Awaga, Observation of spin-gap state in two-dimensional spin-1 kagomé antiferromagnet $m\text{-MPYNN} \cdot \text{BF}_4$, *J. Phys. Soc. Jpn.* **66**, 961 (1997).
- [48] P. Ghosh, J. Seufert, T. Müller, F. Mila, and R. Thomale, Maple leaf antiferromagnet in a magnetic field, *Phys. Rev. B* **108**, L060406 (2023).
- [49] M. Fishman, S. R. White, and E. M. Stoudenmire, The ITensor software library for tensor network calculations, *SciPost Phys. Codebases*, 4 (2022).
- [50] B. Normand and C. Rüegg, Complete bond-operator theory of the two-chain spin ladder, *Phys. Rev. B* **83**, 054415 (2011).
- [51] K. W. Plumb, K. Hwang, Y. Qiu, L. W. Harriger, G. E. Granroth, A. I. Kolesnikov, G. J. Shu, F. C. Chou, C. Rüegg, Y. B. Kim, and Y.-J. Kim, Quasiparticle-continuum level repulsion in a quantum magnet, *Nat. Phys.* **12**, 224 (2016).
- [52] K. Park and S. Sachdev, Bond-operator theory of doped antiferromagnets: From Mott insulators with bond-centered charge order to superconductors with nodal fermions, *Phys. Rev. B* **64**, 184510 (2001).
- [53] P. Ghosh and B. Kumar, Spontaneous dimerization and moment formation in the Hida model of the spin-1 kagome antiferromagnet, *Phys. Rev. B* **97**, 014413 (2018).
- [54] M. Adhikary, A. Ralko, and B. Kumar, Quantum paramagnetism and magnetization plateaus in a kagome-honeycomb Heisenberg antiferromagnet, *Phys. Rev. B* **104**, 094416 (2021).
- [55] Y. Iqbal, D. Poilblanc, R. Thomale, and F. Becca, Persistence of the gapless spin liquid in the breathing kagome Heisenberg antiferromagnet, *Phys. Rev. B* **97**, 115127 (2018).
- [56] H. J. Changlani and A. M. Läuchli, Trimerized ground state of the spin-1 Heisenberg antiferromagnet on the kagome lattice, *Phys. Rev. B* **91**, 100407(R) (2015).
- [57] T. Liu, W. Li, A. Weichselbaum, J. von Delft, and G. Su, Simplex valence-bond crystal in the spin-1 kagome Heisenberg antiferromagnet, *Phys. Rev. B* **91**, 060403(R) (2015).
- [58] F. Haldane, Continuum dynamics of the 1-D Heisenberg antiferromagnet: Identification with the O(3) nonlinear sigma model, *Phys. Lett. A* **93**, 464 (1983).
- [59] I. Affleck, T. Kennedy, E. H. Lieb, and H. Tasaki, Rigorous results on valence-bond ground states in antiferromagnets, *Phys. Rev. Lett.* **59**, 799 (1987).
- [60] P. J. Brown, A. G. Fox, E. N. Maslen, M. A. O'Keefe, and B. T. M. Willis, Intensity of diffracted intensities, in *International Tables for Crystallography*, edited by E. Prince (International Union of Crystallography, Chester, UK, 2006), pp. 554–595.
- [61] M. Troyer, H. Tsunetsugu, and D. Würtz, Thermodynamics and spin gap of the Heisenberg ladder calculated by the look-ahead Lanczos algorithm, *Phys. Rev. B* **50**, 13515 (1994).
- [62] C. Rüegg, B. Normand, M. Matsumoto, C. Niedermayer, A. Furrer, K. W. Krämer, H.-U. Güdel, P. Bourges, Y. Sidis, and H. Mutka, Quantum statistics of interacting dimer spin systems, *Phys. Rev. Lett.* **95**, 267201 (2005).

- [63] W. Zheng, R. R. P. Singh, R. H. McKenzie, and R. Coldea, Temperature dependence of the magnetic susceptibility for triangular-lattice antiferromagnets with spatially anisotropic exchange constants, *Phys. Rev. B* **71**, 134422 (2005).
- [64] Y. J. Kim and R. J. Birgeneau, Monte Carlo study of the $S = \frac{1}{2}$ and $S = 1$ Heisenberg antiferromagnet on a spatially anisotropic square lattice, *Phys. Rev. B* **62**, 6378 (2000).
- [65] K. Wierschem and P. Sengupta, Quenching the Haldane gap in spin-1 Heisenberg antiferromagnets, *Phys. Rev. Lett.* **112**, 247203 (2014).
- [66] C. Yasuda, S. Todo, K. Hukushima, F. Alet, M. Keller, M. Troyer, and H. Takayama, Néel temperature of quasi-low-dimensional Heisenberg antiferromagnets, *Phys. Rev. Lett.* **94**, 217201 (2005).
- [67] J. Schnack, J. Schulenburg, and J. Richter, Magnetism of the $N = 42$ kagome lattice antiferromagnet, *Phys. Rev. B* **98**, 094423 (2018).
- [68] Y. Uekusa and A. Oguchi, Heat capacity of mMPYNN – BF₄, *J. Phys. Soc. Jpn.* **70**, 3464 (2001).
- [69] P. Ghosh, Where is the spin liquid in maple-leaf quantum magnet? [arXiv:2401.09422](https://arxiv.org/abs/2401.09422).
- [70] P. Ghosh, Triplon analysis of magnetic disorder and order in maple-leaf Heisenberg magnet, *J. Phys.: Condens. Matter* **36**, 455803 (2024).
- [71] D. H. Lyons and T. A. Kaplan, Method for determining ground-state spin configurations, *Phys. Rev.* **120**, 1580 (1960).
- [72] T. A. Kaplan and N. Menyuk, Spin ordering in three-dimensional crystals with strong competing exchange interactions, *Philos. Mag.* **87**, 3711 (2007).